Interfacial Bonding between CFRP and Mechanically-Treated Aluminum Liner Surfaces for Risers

Yi Di Boon*, Sunil Chandrakant Joshi, Lin Seng Ong

School of Mechanical and Aerospace Engineering, Nanyang Technological University, Singapore 639789

Abstract

The bonding between metal and carbon fiber-reinforced polymer (CFRP) composites is important in structures such as composite risers. Surface treatment of the metal is required to improve the metal-composite bonding. In this study, the effects of two mechanical surface treatment methods on the bonding between carbon/epoxy composites and aluminum are studied. The treatment methods investigated are grit blasting and grooving. Mechanical tests are performed and the test results are used with finite element simulations to study the failure and damage mechanisms at the composite-metal interface. The mechanical response and damage propagation at the metal-composite interface are modeled successfully using surface-based cohesive behavior. The finite element simulations gave insight into the way that the grooving treatment method improved the composite-metal bonding.

Keywords: Composite-metal interface, Mechanical surface treatment, Composite riser, Finite element analysis, Failure mechanism

1. Introduction

Composite risers are becoming more important in the oil and gas industry as oil production moves increasingly towards deeper waters. The high specific strength of carbon fiber-reinforced polymer (CFRP) composites such as carbon/epoxy allows for smaller platform size and lower tensioner requirements for deep water risers [1]. Composite risers manufactured using the filament winding process consist of the composite body to carry load and an inner liner usually made of metal to prevent leakage. At the liner-composite interface, debonding can lead to fluid pressure build up and subsequently buckling [2]. Therefore,

*Corresponding author
Email address: boon0019@ntu.edu.sg (Yi Di Boon)

it is important to ensure that the bonding at the liner-composite interface is strong.

Various mechanical testing methods have been designed to determine the metal-composite interfacial properties. Metal-composite bonding can be measured by the interlaminar shear strength (ILSS) determined from flexural tests [3, 4, 5]. The interfacial bonding can also be described by the lap shear strength measured by testing the single-lap joint specimen [6]. For the investigation of interfacial fracture, double cantilever beam (DCB) specimens can be tested to determine the fracture energy under mode I loading [7, 8], while single cantilever beam (SCB) specimens can be used for mixed-mode I/II loading [9, 10]. Peel tests have also been used to study the average peel load and assess the adhesion at the metal-composite interface [11].

The bonding between metal and CFRP composites can be improved by performing surface treatment on the metal. Many studies have been conducted to study the effects of different surface treatment methods, including mechanical treatment methods such as grit blasting [12] and mechanical abrasion [3], chemical treatment methods such as etching [8, 13], as well as electrochemical treatment methods such as anodizing [14, 15, 16, 4]. Mechanical treatment methods increase the macro surface roughness of the metal surface leading to moderate metal-composite bonding. They can be coupled with chemical and electrochemical treatment methods to produce micro roughness on the metal surface and achieve strong metal-composite bonding [17, 10].

For filament wound composite risers, the grooving treatment method for the metal liner is proposed. Preliminary results from axial compression tests showed that the grooving treatment can improve the liner-composite bonding compared to the grit blasting treatment [18]. In this study, the underlying reasons for the improvement as well as the associated failure mechanisms for the grooving treatment method are investigated. In addition to axial compression tests, lateral compression tests have also been carried out on the composite pipe specimens. The failure and damage mechanisms at the liner-composite interface treated with grooving and grit blasting are then studied in detail using finite element (FE) simulation tools.

2. Materials and Methodology

2.1. Materials and Fabrication Methods

The composite pipe specimens tested in this study have the same configuration as the previous study [18]. They consist of two components, the aluminum inner liner and the CFRP composite body.

Aluminum liners with an outer diameter of 76.2 mm and a wall thickness of 1.7 mm were used. In order to improve the liner-composite bonding, the liners were treated with grit blasting and grooving. The grit blasting was carried out using coarse sized glass beads (average diameter measuring about 500 μm) supplied by Potters Industries Inc. The surface roughness of the liner was measured using the Taylor-Hobson Talyscan 150 scanning instrument. The inductive

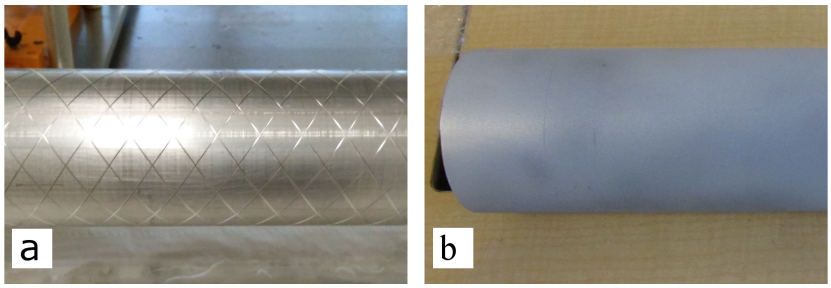

Figure 1: Surface treatment on aluminum liner: (a) grooving, and (b) grit blasting

gauge was used to measure the surface roughness over an evaluation length of 12.5 mm. The arithmetic average roughness values, R_a, of the aluminum liner were 0.543 μm and 3.02 μm before and after grit blasting respectively.

For grooving, round bottomed grooves were cut into the outer surface of the aluminum liner at the angle of $\pm 55^\circ$ to the axial direction. The diameter of the groove bit used was 1 mm. The grooves were 0.2 mm in depth and the groove spacing was 15 mm. The groove depth was set such that the cross sectional area of the resulting grooves is about 50% of the fiber tow area, which is 0.25 mm^2. This ensures that only a fraction of the fiber tow can fit into the grooves so that the structure of the composite layers are not significantly disrupted. The spacing of 15 mm was calculated from five times the width of the fiber tow, which is 3 mm. The resulting groove pattern covers about 10% of the liner surface. Using a multiple of the fiber tow width for the groove spacing helps to align the fiber tows to the grooves for filament winding. Figure 1 shows the resulting liner surfaces after the grooving and grit blasting treatments.

Carbon/epoxy composite was used for the fabrication of the composite pipes. The Epolam 5015/5015 epoxy system supplied by Axson Technologies was used as the matrix while the HexTow® IM2A carbon fibers supplied by Hexcel Corp were used as the reinforcement. The representative composite pipes were fabricated using the filament winding process. Before the winding process, the surface treated aluminum liners were cleaned using soap and water to remove dust and grease. After allowing the liners to dry, the composite layers were wound onto the outer surface of the liners. Three helical layers with the angle $\pm 55^\circ$ to the axial direction make up the composite layers. The composite pipes were cured at room temperature for 24 hours followed by 16 hours post-cure at 80°C. The composite pipes were rotated throughout the curing process to produce composite pipes with near uniform wall thickness. The composite layers on the resulting pipe specimens were 1 mm thick in total. Table 1 gives a summary of the different specimen types investigated in this study.

For the composite pipe specimens with aluminum liner treated with grooving, microscope examination of the liner-composite interface show that some of the grooves contain both carbon fiber and epoxy while some grooves are only filled with epoxy (Figure 2) [18].

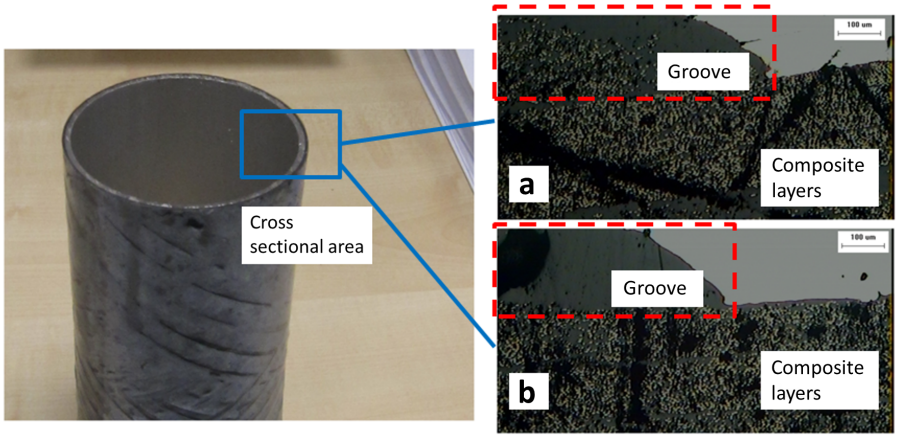

Figure 2: The cross sectional areas around two different grooves examined under a microscope: (a) groove with carbon fiber, (b) groove without carbon fiber

Table 1: Summary of test specimens

Specimen type	Pipe label	Liner outer diameter (mm)	Liner thickness (mm)	Composite thickness (mm)
Aluminum liner	Al	76.2	1.7	0
Composite pipe with aluminum liner treated with grit blasting	GB-C	76.2	1.7	1
Composite pipe with aluminum liner treated with grooving	GR-C	76.2	1.7	1

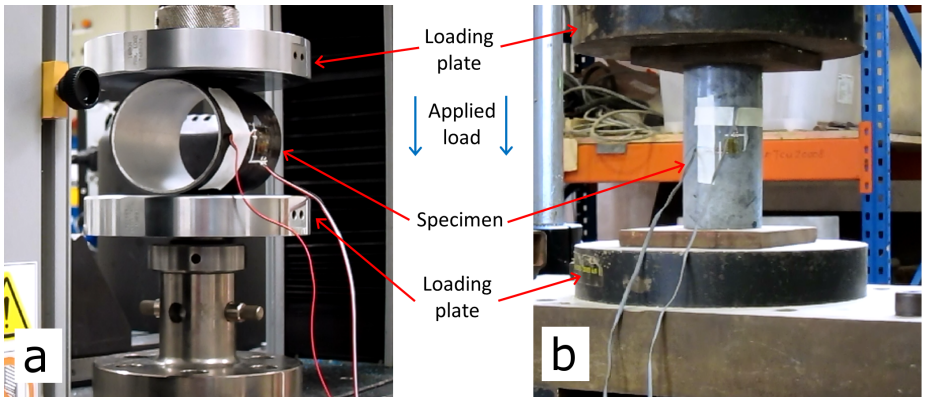

Figure 3: Compression tests: (a) lateral compression test, and (b) axial compression test

Table 2: Summary of mechanical tests

Mechanical test		Specimen type		
		Al	GB-C	GR-C
Axial compression test	Specimen length (mm)	150	150	150
	Number of specimen	1	3	3
Lateral compression test	Specimen length (mm)	120	120	120
	Number of specimen	1	3	3

2.2. Mechanical Tests

Lateral and axial compression tests were carried out on the aluminum liner and composite pipe specimens. Figure 3 shows the experimental setup for the two compression tests. Both compression tests were carried out at a constant head displacement rate of 1.3 mm/min. For the lateral compression test, the Instron 5569 universal testing machine (UTM) was used. The lateral compression test specimens were cut to a length of 120 mm. Load and head displacement data were recorded from the UTM. The lateral compression tests were performed following the ASTM D2412 standard. For the axial compression test, loads above 100 kN were required, thus the Instron 8506 UTM was used. The length of the axial compression test specimens was 150 mm. Besides load and head displacement data, axial and hoop strains were also recorded using strain gauges attached to the middle of the specimens. The ASTM D695 standard was followed closely when performing the axial compression tests. While carrying out the mechanical tests, the test specimens were observed closely for any visual and audible sign of failure. The number and type of specimens tested are shown in Table 2.

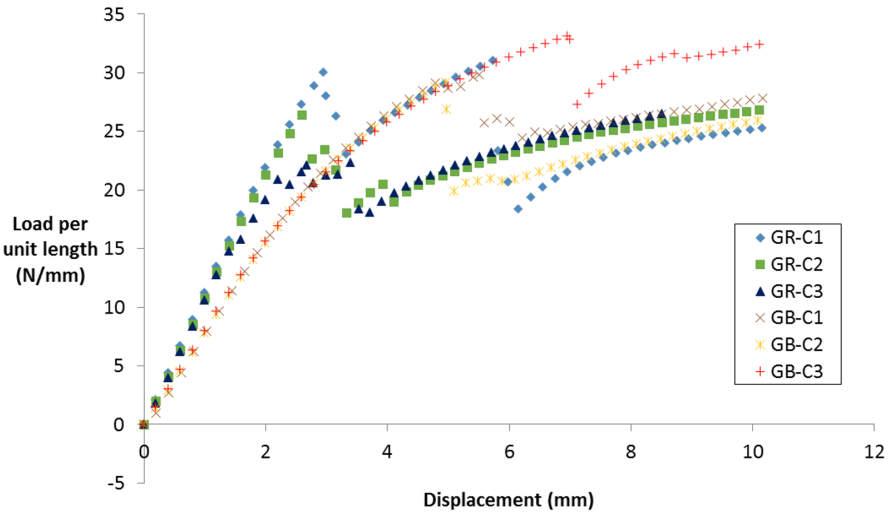

Figure 4: Load-displacement plots for lateral compression tests on composite pipe specimens with liner

3. Experimental Results

3.1. Lateral Compression

Figure 4 shows the load-displacement curves from the lateral compression tests on composite pipe specimens with liner. The load per unit length is plotted to account for the small differences in length between the pipe specimens. From the load displacement data, the pipe stiffness (PS) can be determined from the slope of the graph at small displacements (below 2.5 mm).

From the load-displacement curve, the average pipe stiffness for the composite pipes with aluminum liner treated with grooving (specimens labeled GR-C) was obtained as 10.71 MPa. This is higher than the average pipe stiffness of composite pipes with aluminum liner treated with grit blasting (specimens labeled GB-C), which is 7.76 MPa.

For the lateral compression tests, the first evidence of failure was a cracking sound which lasted for a fraction of a second. This coincided with the sharp drop in the load-displacement curve. At this stage, there was no visible damage to the liner and the composite layers. Therefore, the cracking sound indicated that failure initiation has occurred at the liner-composite interface. The interface failure initiation for the GR-C specimens occurred at a lower load and displacement compared to the GB-C specimens.

After the first failure, there are several smaller peaks in the load-displacement graphs for both GB-C and GR-C specimens, but more so for GR-C specimens. The smaller peaks are the result of the interface damage not propagating simultaneously in all directions. This shows that the liner-composite interface is not completely uniform for the specimens tested. Also, there may be some minor

Table 3: Summary of lateral compression test results for composite test specimens with liner

	Composite pipe with aluminum liner treated with grit blasting	Composite pipe with aluminum liner treated with grooving	% Difference
Pipe specimen label	GB-C	GR-C	
Pipe stiffness (MPa)	7.76 ± 0.06	10.71 ± 0.23	+38.0
Load at first failure (N/mm)	30.7 ± 2.1	26.2 ± 4.0	-14.7
Displacement at first failure (mm)	5.81 ± 1.03	2.75 ± 0.19	-52.7

fiber breakage in the composite layers at this stage resulting in some barely visible damage. At displacements greater than 8 mm, the damage propagation at the liner-composite interface is mostly complete and both the GB-C and GR-C specimens showed a similar load-displacement response.

In order to compare the two treatment methods, the percentage difference between the GB-C and GR-C properties is calculated using equation 1:

$$\%Difference = \left(\frac{P_{GR-C}}{P_{GB-C}} - 1\right) \times 100\% \quad (1)$$

where P_{GR-C} and P_{GB-C} are the mechanical properties of the GR-C and GB-C specimens respectively. Table 3 shows a comparison of the lateral compression test results for the GR-C and GB-C specimens.

Figure 5 shows the damage on the specimens after the lateral compression tests. Debonding at the liner-composite interface was observed for both GR-C and GB-C specimens. For the GB-C specimens, matrix cracking can also be seen at the top part of the specimen. This was not the case for the GR-C specimens.

3.2. Axial Compression

The axial compression test results have been discussed in the previous study [18] and is shown in Figure 6. The initial stress-strain response of the specimens was linear elastic. The GB-C specimens, with average axial elastic modulus of 35.5 GPa, were slightly stiffer than the GR-C specimens, with average axial elastic modulus of 31.6 GPa. A reduction in the stiffness occurred at compressive stresses of around 100 MPa and 120 MPa for the GB-C and GR-C specimens respectively. Comparing the stress-strain response of the composite pipe specimens to that of the aluminum liner (Figure 7), it can be seen that this stiffness reduction is due to the liner yielding.

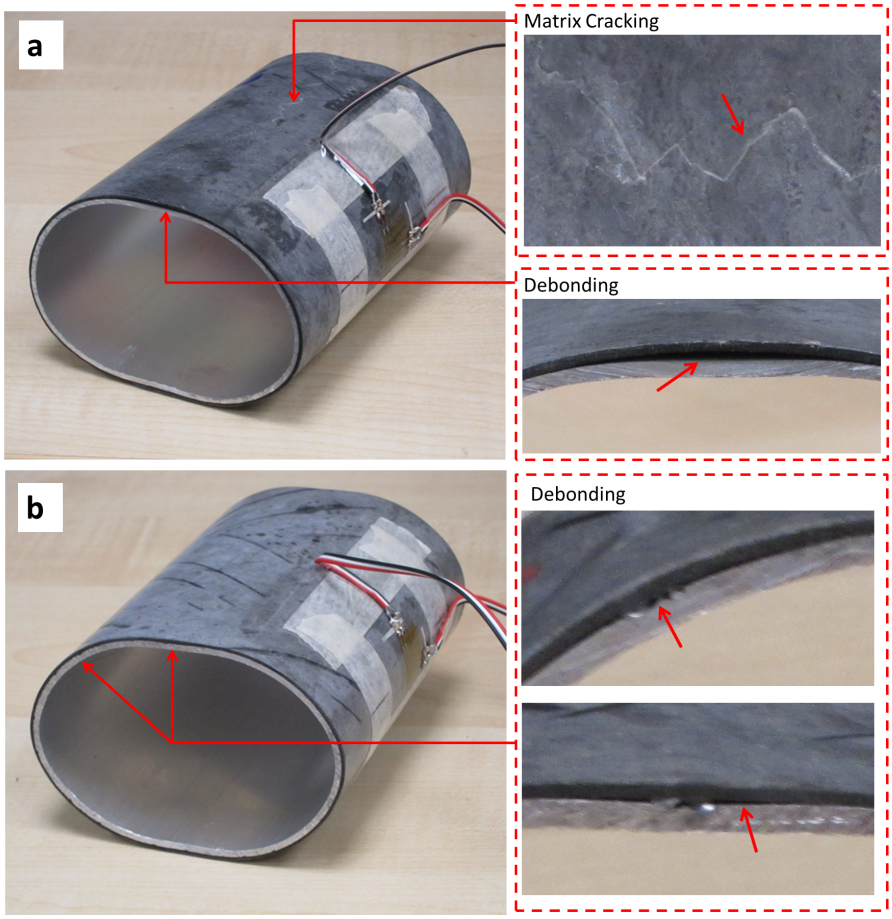

Figure 5: Damage on composite pipe specimens with liner after lateral compression test: (a) specimen with liner treated with grit blasting; (b) specimen with liner treated with grooving

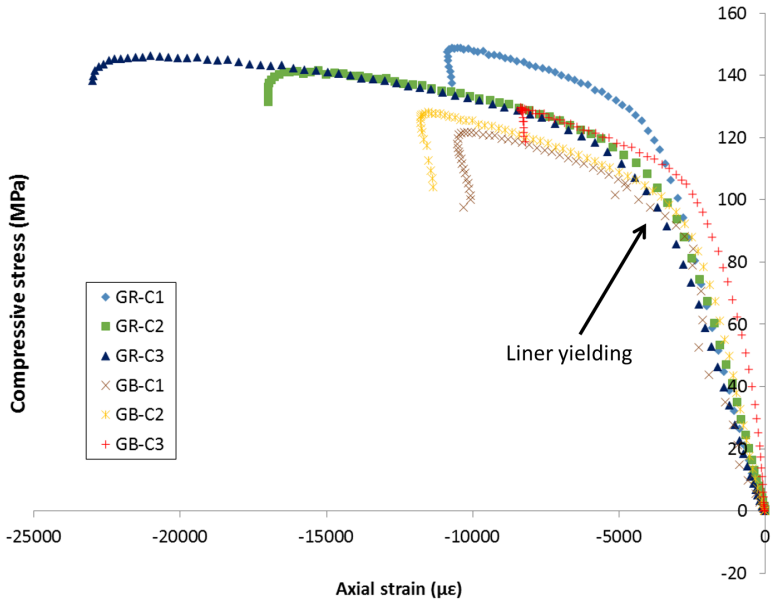

Figure 6: Compressive stress vs axial strain graphs for axial compression tests on composite pipe specimens with liner

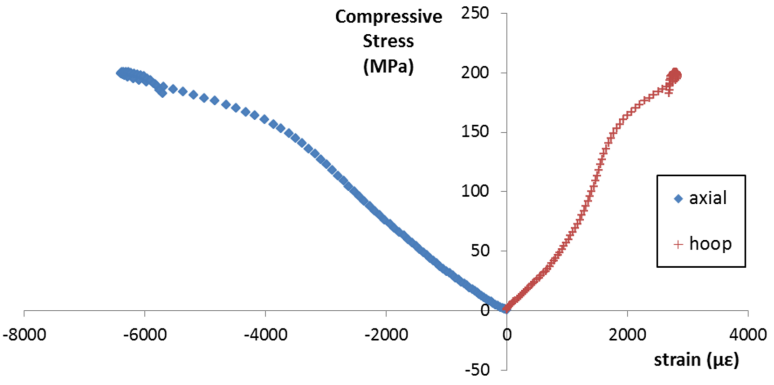

Figure 7: Axial compression test results for aluminum liner

Figure 8: Bulging at one end of a composite pipe specimen after axial compression test

Final failure is determined when the load on the specimens stops to increase with increasing deformation. At final failure, bulging of the specimens around the circumference was observed (Figure 8). This suggests that debonding at the liner-composite interface occurred at final failure. The average maximum compressive stress was 145.6 MPa for GR-C specimens and 126.6 MPa for GB-C specimens. A summary of the axial compression test results is shown in Table 4.

4. Finite Element Simulations and Discussions

4.1. Characterization of Aluminum Liner

The yielding and plastic deformation of the aluminum liner are important aspects in the failure analysis of the composite pipe specimens. Therefore, characterization of the aluminum was carried out to ensure the behavior of the liner is simulated accurately. The elastic modulus and yield stress of aluminum was obtained from available material data. For the plastic deformation of aluminum, characterization of the aluminum liner was carried out. The characterization was performed using a similar method to the method described by Rathnaweera et al. [19]. The lateral compression test data on the aluminum liner were used. The plastic deformation of aluminum was determined by fitting the FE simulation of the lateral compression test to the experimental results. For the FE

Table 4: Summary of axial compression test results for composite test specimens with liner

	Composite pipe with aluminum liner treated with grit blasting	Composite pipe with aluminum liner treated with grooving	% Difference
Pipe specimen label	GB-C	GR-C	
Axial linear elastic modulus (GPa)	35.3 ± 3.09	31.6 ± 2.78	-10.5
Maximum compressive stress (MPa)	126.6 ± 4.24	145.6 ± 3.83	+15.0
Axial strain at failure ($\mu\epsilon$)	-10198 ± 1729	-16945 ± 6066	+66.0

Table 5: Material properties of the aluminum liner

	E (GPa)	ν	Initial yield stress, σ_Y (MPa)	Exponent N
Aluminum	69	0.33	201	0.08

simulation, yielding was determined by the von Mises criterion and plasticity was modeled using a power law given by equation 2 [20]:

$$\frac{\sigma_r}{\sigma_Y} = \left(\frac{\sigma_r}{\sigma_Y} + \frac{3G}{\sigma_Y} \bar{\epsilon}^p \right)^N \tag{2}$$

where σ_r is the current yield stress, σ_Y is the initial yield stress, G is the material shear modulus, $\bar{\epsilon}^p$ is the accumulated equivalent plastic strain, and N is the exponent where $0 < N < 1$. The plasticity model in equation 2 was chosen because it can model the plastic deformation of aluminum well while only requiring one additional parameter, the exponent N. The lateral compression experimental and simulation results are shown in Figure 9. The value of 0.08 for the exponent N was found to give a good fit. The FE simulation also validates the elastic modulus and yield stress values of the aluminum. The mechanical properties for the aluminum liner are shown in Table 5.

4.2. Composite Pipe Simulation Setup

Finite element simulations were carried out using Abaqus version 6.14 [21]. The representative composite pipe with liner was modeled using the SC8R 8-node hexahedron continuum shell elements. The SC8R element is suitable for simulations of thin to moderately thick shell structures. Also, the 3-D geometry of the SC8R element allows for better contact modeling compared to 2-D

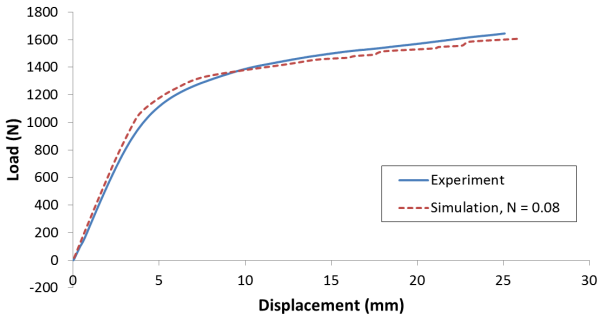

Figure 9: Aluminum liner lateral compression load-displacement curves from experiment and simulation

Table 6: Material properties of the carbon/epoxy composite

	E_1 (GPa)	E_2 (GPa)	ν_{12}	G_{12} (GPa)
Carbon/epoxy	128.5	10.8	0.3	2.7

Note: subscripts 1 and 2 denote the fiber and transverse directions respectively

conventional shell elements. The layered section definition with three integration points per layer is used with the shell elements to model the carbon/epoxy composite layers. The material properties of the carbon/epoxy composite were computed from the constituent material properties using the rule of mixture and the Halpin-Tsai equations [22]. The composite properties are shown in Table 6.

The surface-based cohesive behavior available in Abaqus is used to model the liner-composite interface. The traction-separation behavior at the interface before damage is described using a linear elastic model. The normal and shear components are assumed to be uncoupled. The traction-separation behavior is then given by equation 3 [21]:

$$\boldsymbol{\tau} = \begin{Bmatrix} \tau_1 \\ \tau_2 \\ \tau_3 \end{Bmatrix} = \begin{bmatrix} K_{11} & 0 & 0 \\ 0 & K_{22} & 0 \\ 0 & 0 & K_{33} \end{bmatrix} \begin{Bmatrix} \delta_1 \\ \delta_2 \\ \delta_3 \end{Bmatrix} = \boldsymbol{K\delta} \tag{3}$$

where τ_i is the interface traction, δ_i is the interface separation, K_{ij} is the interface stiffness, and indices i, j = 1,2 denote the shear directions, 3 denote the normal direction.

The damage response of the surface-based cohesive behavior is similar to the model described by Camanho et al. [23]. Damage initiation was determined by the quadratic traction criterion. A linear softening law based on energy dissipated was used for the post-damage behavior. The damage propagation was determined using the B-K criterion. The value of 1.6 was used for the η parameter in the B-K criterion. This value has been found to give good predictions for carbon/epoxy composites [24]. The overall traction-separation

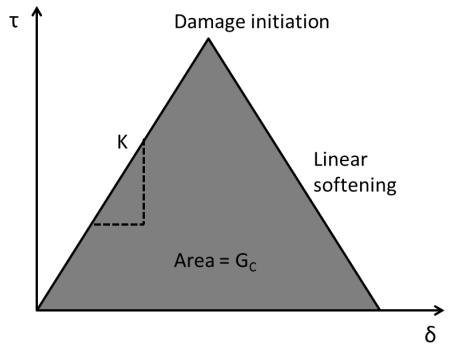

Figure 10: Traction (τ) vs separation (δ) response of the surface-based cohesive behavior for the liner-composite interface. K is the interface stiffness and G_C is the critical energy release rate.

response for the surface-based cohesive behavior is illustrated in Figure 10.

The interfacial properties of the liner-composite interface are largely dependent on the epoxy resin. Therefore, the liner-composite interface was assumed to behave similar to a homogenous material, that is, interface stiffness, K and traction at onset of damage, τ^o are assumed to be the same in all directions. For the critical energy release rate, $G_{IIC} = G_{IIIC} = 2G_{IC}$ was initially assumed. The values for K, τ^o, G_{IC}, G_{IIC} and G_{IIIC} were then determined by fitting the simulation results for the lateral compression test to the experimental result. This approach is used because the curved liner-composite interface in the composite pipe specimens makes measuring the interfacial properties directly from mechanical testing difficult. The fitting approach allows the interfacial properties to be determined by comparing FE simulation results to data that can be measured more easily in experiment, such as the load-displacement and stress-strain responses. However, the FE simulations need to be repeated many times to obtain a good fit and to ensure the interfacial properties are accurate.

4.3. Lateral Compression (Simulation)

The finite element mesh for the simulation of the lateral compression tests is shown in Figure 11. The green component is the aluminum liner and the blue component is the carbon/epoxy composite. The loading plates were modeled using rigid surfaces. The three helical composite layers were assumed to be perfectly bonded together. The displacement of the top plate was controlled to compress the composite pipe. Other boundary conditions for the simulation are shown in Figure 11. The composite pipe specimen was modeled with 28800 elements and 49005 nodes. The mesh size was chosen based on a mesh convergence study where the number of elements was varied from 4800 to 42000.

For the simulation results, the percentage error is calculated using equation 4:

$$\%Error = \left(\frac{P_{sim}}{P_{exp}} - 1\right) \times 100\% \tag{4}$$

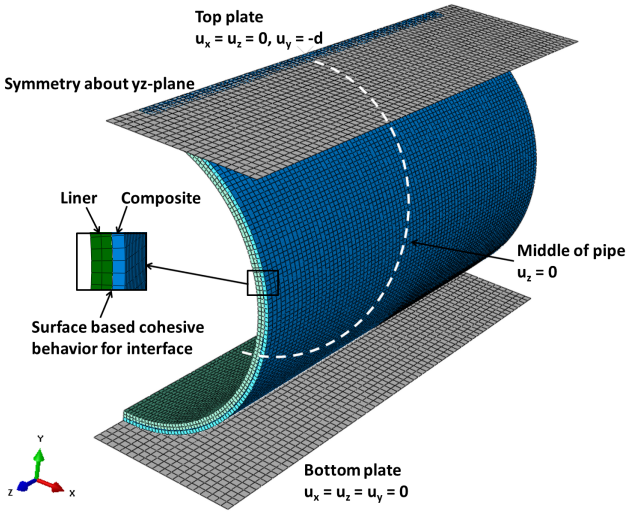

Figure 11: Finite element mesh and boundary conditions for lateral compression simulations (u_i denotes displacement in the i direction)

where P_{sim} is the simulation value and P_{exp} is the experimental value.

The values for interface stiffness, K and traction at onset of failure, τ^o were varied to fit the simulations to experimental results. The fitting process can be carried out systematically as K and τ^o affected different aspects of the load-displacement response, that is, K affected the pipe stiffness whereas τ^o affected the onset of failure. An initial value of 10^{15} Pa/m was used for K. This stiffness value was used by Camanho et al. to simulate the delamination of carbon/epoxy laminates, and is expected to be higher than required for the simulation of the liner-composite interface [23]. The value of K is then reduced from the initial value to fit the pipe stiffness from the simulations to the experimental results. After obtaining K, the value for τ^o can be determined from the contact stresses at the point of interface failure initiation in the simulations. After failure initiation, the interface damage propagation in the simulations is controlled by the critical energy release rate. From experiments, the failure at the liner-interface occurred suddenly (similar to brittle failure). This allows the critical energy release rate to be estimated as $\frac{1}{2}K(\tau^o)^2$. The values for the critical energy release rate were then adjusted to obtain a good fit for the load-displacement response after the failure initiation at the interface. Figure 12 shows the load-displacement curves from the simulations compared to experiments. A comparison of some of the properties calculated from simulations to their experimental counterparts is given in Table 7. The K, τ^o, G_{IC}, G_{IIC} and G_{IIIC} values fitted to experimental results are given in Table 8. Figure 13 gives a comparison of the interfacial behavior for the two surface treatment methods studied under mode II loading.

The grooving surface treatment (GR-C specimens) resulted in both higher

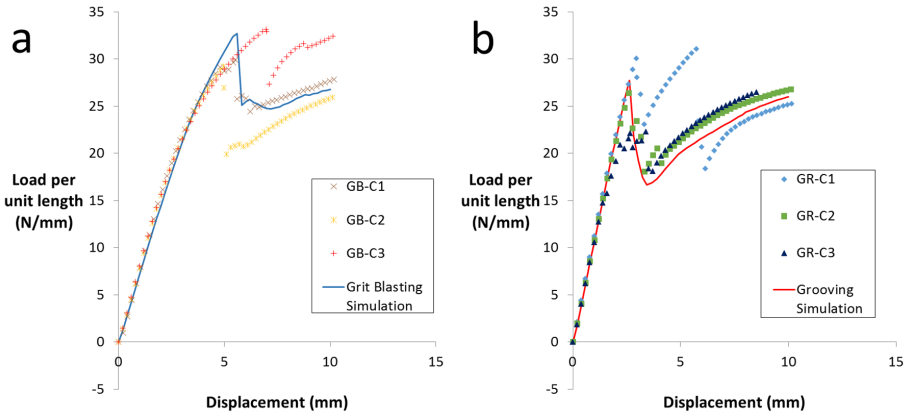

Figure 12: Lateral compression simulation and experimental results: (a) composite pipe with liner treated with grit blasting; (b) composite pipe with liner treated with grooving

Table 7: Comparison of simulation and experimental results for the lateral compression test on composite pipe specimens with liner treated with grit blasting and grooving

Surface treatment	Grit blasting			Grooving		
Specimen label	GB-C			GR-C		
	Exp	Sim	% Error	Exp	Sim	% Error
Pipe stiffness (MPa)	7.76 ±0.06	7.19	-7.3	10.71 ±0.23	10.78	+0.7
Load at first failure (N/mm)	30.7 ±2.1	32.7	+6.5	26.2 ±4.0	27.7	+5.7
Displacement at first failure (mm)	5.81 ±1.03	5.60	-3.6	2.75 ±0.19	2.61	-5.1

Note: Exp = Experiment, Sim = Simulation

Table 8: Interface properties used in simulations

Surface treatment	Grit blasting	Grooving
Interface stiffness, K (Pa/m)	6×10^{10}	4×10^{11}
Traction at onset of failure, τ^o (MPa)	5	6
G_{IC} (Pa·m)	210	60
G_{IIC} and G_{IIIC} (Pa·m)	230	110

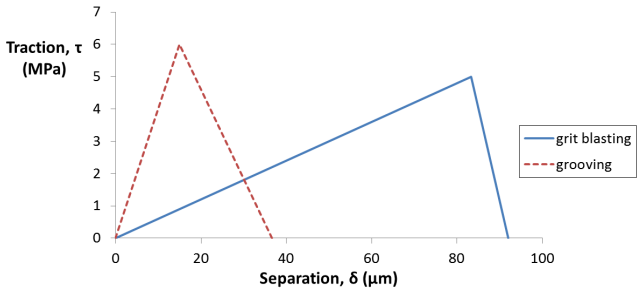

Figure 13: Comparison of the interfacial traction-separation response for grit blasting and grooving under mode II loading

interface stiffness, K and traction at onset of damage, τ^o compared to grit blasting (GB-C specimens). For the grit blasting treatment, the low value of K means that some sliding at the liner-composite interface can occur. This coupled with the yielding of the aluminum liner resulted in the nonlinear load-displacement response close to the failure initiation for the GB-C specimens. In contrast, the grooving treatment produced an interface with high stiffness K and resulted in the load-displacement response being close to linear before failure. The higher K for grooving also caused higher tractions at the liner-composite interface when lateral load is applied. This led to the GR-C specimens failing at a lower applied load (26.2 N/mm) compared to GB-C specimens (30.7 N/mm) even though the τ^o for grooving was higher. From the lateral compression experiments, matrix cracking was observed for the GB-C specimens but not for GR-C specimens (Figure 5). This is due to the difference in the damage propagation at the interface. Figure 14 shows the debonding and damage propagation at the liner-composite interface from the simulations. The area that has debonded is shown in red and the damage propagation direction is shown by the white arrows. The plots were taken at displacements of 6 mm and 9 mm for the GB-C specimens, and at displacements of 3 mm and 9 mm for the GR-C specimens. The grit blasting surface treatment resulted in a more compliant liner-composite interface and thus slower damage propagation. As a result, the composite layers were still bonded to the liner at the top part of the GB-C specimen (blue region at the top in Figure 14(a)) after damage has occurred at the liner-composite interface at the sides. The load sharing between liner and composite at the top part of the specimen resulted in higher stresses in the composite and led to matrix cracking. For the grooving surface treatment, the damage propagation occurred more quickly (Figure 14(b)). Therefore, the stresses in the composite were lower and matrix cracking did not occur for the GR-C specimens.

The traction at onset of failure τ^o for the grit blasting and grooving treatment methods were similar to the epoxy-aluminum adhesion strengths measured by Sharifi Golru et al. [13]. In their study, the aluminum surface was chemically treated. The epoxy-aluminum adhesion strengths of 5.6 MPa was obtained with the alkaline etching treatment and a higher strength of 6.3 MPa was achieved

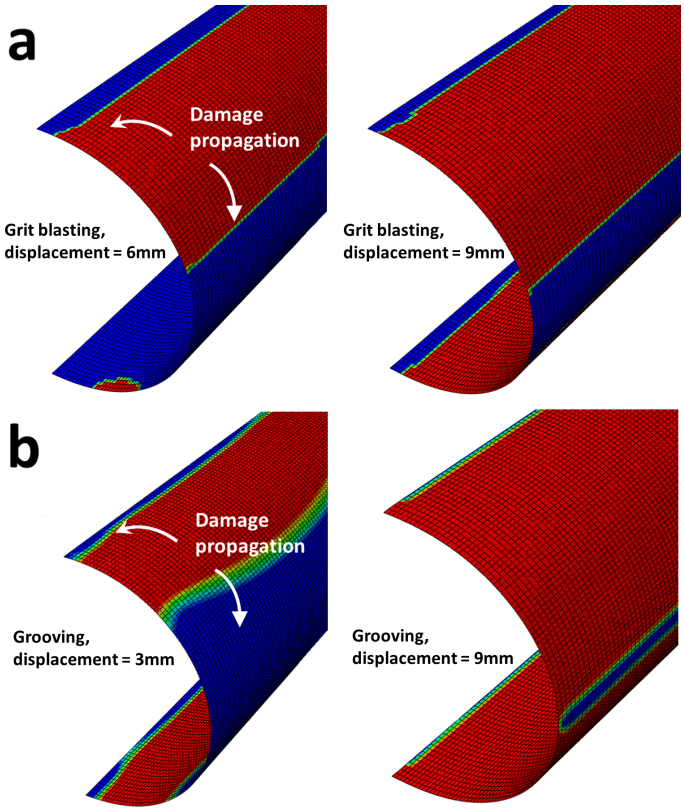

Figure 14: Liner-composite debonding (shown in red) from lateral compression simulations: (a) specimen with grit blasting treatment; (b) specimen with grooving treatment

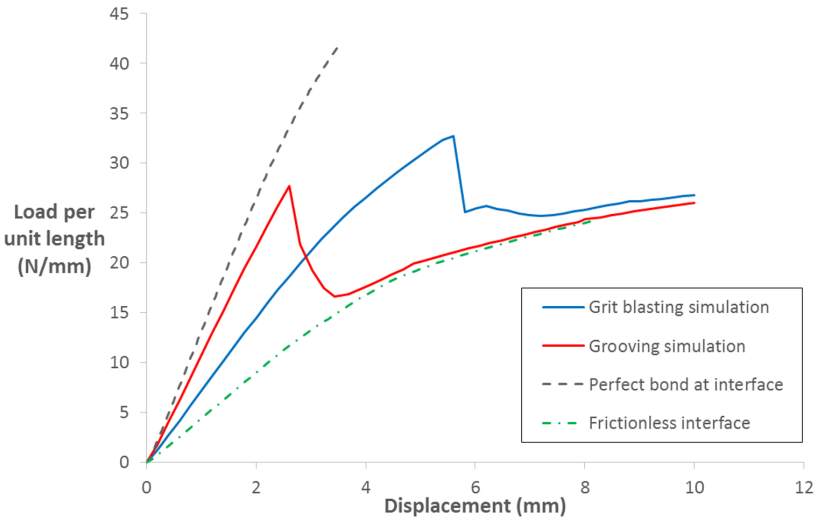

Figure 15: Comparison of lateral compression simulations with different interaction properties at the liner-composite interface

with treatment using a zirconium (Zr) based solution. Sharifi Golru et al. also reported the surface roughness produced by alkaline etching and the zirconium coating treatment as 0.430 μm and 0.520 μm respectively. Despite the surface roughness obtained using grit blasting in this study being higher (3.02 μm), the resulting strength was slightly lower than that of the alkaline etching treatment from Sharifi Golru et al. This can be due to the grit blasting method producing macro surface roughness which is less effective in improving the metal-composite bonding [17].

In order to further study the effects of liner-composite interface properties on the lateral compression tests, simulations with the liner-composite interface having perfect bonding and frictionless contact were also carried out. A comparison of the simulation results with different properties at the liner-composite interface is shown in Figure 15. The simulations with perfect bonding and frictionless contact give the upper and lower bounds for the load-displacement response. It can be seen that the pipe stiffness for the specimens with grooving is very close to that of perfect bonding. This is because the mechanical interlock due to the grooves prohibits slipping at the liner-composite interface. After failure, the specimens with grooving and grit blasting both behaved very similarly to having frictionless contact at the liner-composite interface.

4.4. Axial Compression (Simulation)

As discussed in section 3.2, the surface treatment method affected the yielding of the aluminum liner. In order to reproduce this effect in FE simulations, the plastic deformation of the liner needs to be examined further.

From the axial compression test of aluminum liner (shown in Figure 7), the apparent elastic modulus of aluminum is 43.4 GPa. This value is much lower than the actual modulus of the aluminum (69 GPa). This difference can be explained by the findings of Liu et al. [25]. The lower modulus value from the axial compression test is caused by stress concentration in the specimen resulting in the early yielding of some parts of the specimen. Stress concentration in the specimen can be caused by factors such as friction or an uneven contact surface between the loading plates and the specimen due to imperfections at the ends of the specimen.

This stress concentration is related to the aspect ratio of the specimen [25]. As the composite pipe specimens have a similar aspect ratio as the aluminum pipe specimen, the stress concentration effect in the aluminum liner is expected to be present for the axial compression tests on the composite pipe specimens as well. As will be shown later in this section, varying the interfacial parameters K, τ^o, G_{IC} and G_{IIC} of the composite pipe model has little effect on the stress distribution and yielding behavior of the liner. In order to account for the stress concentration effect in simulations, it is essential to change the model of the liner body. To achieve this, two approaches were considered: (i) the slanted contact model and (ii) the sandwich model.

Figure 16(a) shows the finite element mesh for the slanted contact model. The boundary conditions for the axial compression simulations using this model are also shown. The mesh for the composite pipe consists of 48000 elements and 81305 nodes. This was chosen based on a mesh convergence study where the number of elements was changed from 4800 to 54000. The liner is shown in green and the composite is shown in blue. The specimen is modeled with uneven height such that the contact between the loading plate (modeled as a rigid surface) and the axial compression specimen occurs at a small angle. The contact angle was calculated using the method introduced by Liu et al. [25]. Using the apparent elastic modulus of 43.4 GPa from the axial compression test on the aluminum liner, the contact angle of 0.346° was determined. The stress distribution in the aluminum liner as a result of the stress concentration in the slanted contact model is shown in Figure 16(b). The side with the larger height had higher stress when compressed.

The second approach is the sandwich model shown in Figure 17. The finite element mesh and boundary conditions for the model are shown in Figure 17(a). The mesh for the sandwich model has 32000 elements and 57477 nodes. The number of elements required was determined from a mesh convergence study where the number of elements was increased from 3720 to 43200. The two ends of the sandwich model are the soft segments which are considered to have fully yielded and have an effective modulus of 1.5 GPa. This value was determined from the stress-strain response of aluminum after yielding. On the other hand, the hard segment in the middle has the properties of normal aluminum as determined in the characterization of the aluminum liner (Table 5). The soft segments are colored orange, the hard segment is colored green and the composite is colored blue in Figure 17(a). The total volume fraction of the soft segment was determined as 0.0112 using the findings of Liu et al. and the ap-

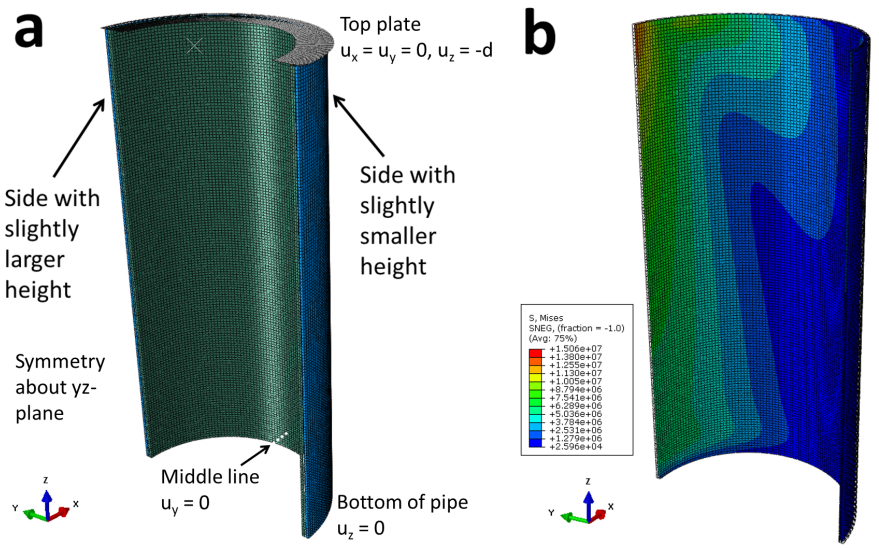

Figure 16: Slanted contact model for axial compression simulation: (a) finite element mesh and boundary conditions (u_i denotes displacement in the i direction), (b) liner stress distribution

parent elastic modulus of 43.4 GPa [25]. For the sandwich model, homogeneous deformation was assumed in the axial direction. The stress distribution in the aluminum liner modeled using this approach is shown in Figure 17(b). Unlike the slanted contact model, the plastic deformation in the liner was contained in the soft segments and the stresses are more uniform.

The two models are used to simulate two different ways that the liner can be affected by stress concentration while producing the same apparent elastic modulus. For the slanted contact model, the stress concentration originates at the side with slightly larger height and gets distributed from there over the entire liner. On the other hand, for the sandwich model, the stress concentration results in the yielding at the ends of the liner (modelled as the soft segments) while the middle region is largely unaffected. The difference in the volume of the liner affected by stress concentration between the two models leads to different applied loads where the liners in the models yield completely. The liner in the slanted contact model is expected to yield completely at a lower load compared to the sandwich model.

For the grit blasting treatment method (GB-C specimens), the treated liner surface is homogeneous in the macroscopic scale. From lateral compression simulations (section 4.3), the liner-composite bonding for GB-C specimens was found to have low interface stiffness allowing sliding between the liner and composite while bonded. Therefore, for the axial compression tests of GB-C specimens, the stress concentrations near the loading regions are expected to affect the entire height of the liner. Hence, for the simulation of axial compression tests on the GB-C specimens, the slanted contact model was used. For the composite-liner

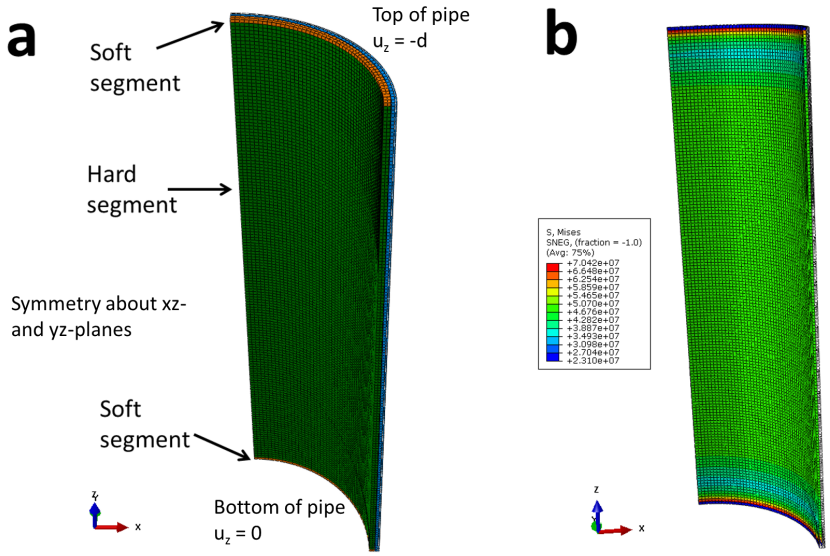

Figure 17: Sandwich model for axial compression simulation: (a) finite element mesh and boundary conditions (u_i denotes displacement in the i direction), (b) liner stress distribution

bonding, the liner-composite interface properties for the grit blasting treatment determined from lateral compression simulations were used (Table 8). The simulation results obtained were in good agreement with the experimental results (Figure 18). This shows that the choice of using the slanted contact model to simulate the axial compression tests for the GB-C specimens was appropriate. After the liner has fully yielded, the carbon/epoxy composite body became the main load bearing component. Final failure in the axial compression test occurred when matrix compression failure took place in the composite. This was followed by debonding at the liner-composite interface that was also observed in experiments (Figure 8).

For the composite pipe specimens with liner treated with grooving (GR-C specimens), the complete yielding of the liner occurred at a higher load compared to the GB-C specimens (Figure 6). This indicates that the grooving treatment method changed the yielding behavior in the liners of the GR-C specimens. In order to study the yielding behavior, three simulations were carried out with different methods of modeling the aluminum liner. The simulation results are shown in Figure 19. In all three simulations, the liner-composite interface was modeled using the interface properties for the grooving treatment determined from the lateral compression simulations (Table 8). For grooving simulation 1, the sandwich model was used whereas for grooving simulation 2, the slanted contact model was used. The complete yielding of the aluminum liner for grooving simulation 1 occurred at a higher compressive stress (about 120 MPa) compared to grooving simulation 2 (about 90 MPa) due to plastic deformation initially being contained in the soft segments of the sandwich model. For grooving sim-

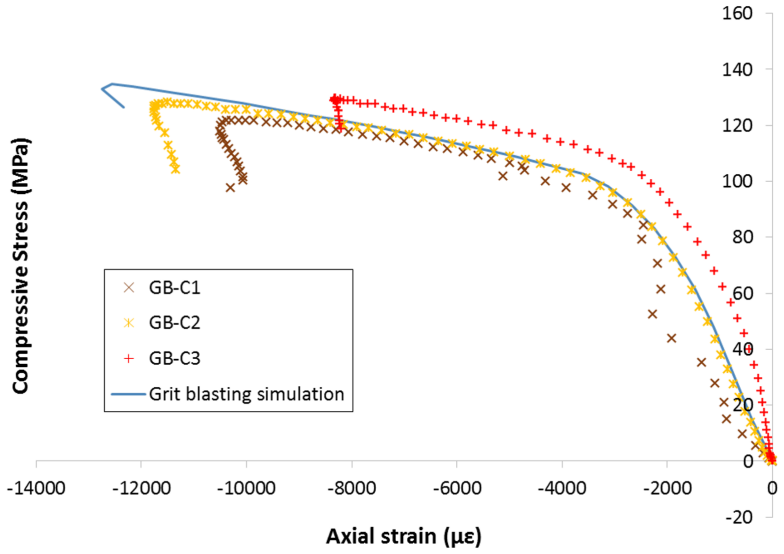

Figure 18: Axial compression simulation and experimental results for composite pipe with liner treated with grit blasting

ulation 2 (Figure 19), the compressive stress when complete yielding occurs is similar to that of the GB-C simulation (Figure 18). This shows that, as mentioned earlier in the section, the interfacial properties K, τ^o, G_{IC} and G_{IIC} do not affect the yielding behavior of the liner significantly. From Figure 19, it can be seen that grooving simulations 1 and 2 give the upper and lower boundaries for the stress-strain response in the axial compression tests of the GR-C specimens. In particular, the stress-strain response from grooving simulation 1 was very close to the experimental data for the GR-C1 specimen.

For grooving simulation 3 in Figure 19, a combination of the sandwich model and slanted contact model was used. The model was constructed using the contact angle of 0.173° which is half of the value calculated previously. The liner was also modeled with a soft segment of volume fraction 0.00559 which is again half of the value earlier, resulting in an apparent elastic modulus of 55.1 GPa for the aluminum liner. The model for grooving simulation 3 is therefore a combination of 50% of the slanted contact model and 50% of the sandwich model. Using this combination, the stress-strain response from grooving simulation 3 agreed well with the average stress-strain response from experiments for the GR-C specimens (Figure 19). For final failure, the damage mechanism was similar to the specimens with grit blasting, which is matrix compression damage in the carbon/epoxy composite followed by debonding at the liner-composite interface.

A summary of the axial compression simulation results for both GB-C and GR-C specimens is shown in Table 9.

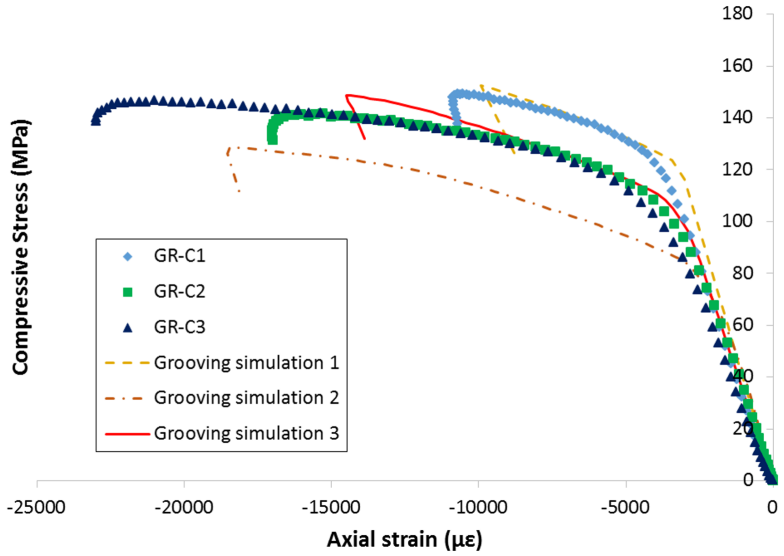

Figure 19: Axial compression simulation and experimental results for composite pipe with liner treated with grooving

Table 9: Comparison of simulation and experimental results for the axial compression test on composite pipe specimens with liner treated with grit blasting and grooving

Surface treatment	Grit blasting			Grooving		
Specimen label	GB-C			GR-C		
	Exp	Sim	% Error	Exp	Sim	% Error
Axial linear elastic modulus (GPa)	35.3 ±3.1	38.2	+8.2	31.6 ±2.8	33.9	+7.3
Maximum compressive stress (MPa)	126.6 ±4.2	134.7	+5.9	145.6 ±3.8	148.7	+2.1

Note: Exp = Experiment, Sim = Simulation

4.5. Discussion on the Grooving Surface Treatment

The axial compression simulations of the GR-C specimens show that the grooving treatment method led to stress concentration only affecting a limited portion of the aluminum liner. Microscopic inspection of the grooves showed that some of the grooves contain carbon/epoxy composite while others are only filled with epoxy (Figure 2). After yielding, the stiffness in the axial direction of the aluminum liner is similar to that of the epoxy used in this study, but much smaller than that of the carbon/epoxy composite. Therefore, the stiffer carbon/epoxy composite in the grooves can act as reinforcement to the aluminum liner.

The effect of the grooving treatment method is further illustrated in the schematic diagram shown in Figure 20. The plastic flow in the schematic diagram indicates the region of the liner that has yielded. For the aluminum liner affected by stress concentration, the carbon/epoxy composite in the grooves can work to redistribute the stresses more evenly to other parts of the liner and the composite body. In Case 1, all the grooves contain both carbon fiber and epoxy. As a result, only a small portion of the liner experience early yielding due to the stress concentration. The liner in this case can be modeled using the sandwich model (grooving simulation 1 in Figure 19).

In Case 2 of Figure 20, some of the grooves only contain epoxy, which is ineffective as reinforcement for the liner. This results in a larger portion of the liner affected by early yielding due to the stress concentration. The effect of the grooves in Case 2 on the liner is similar to modeling the liner with a combination of the sandwich model and the slanted contact model (grooving simulation 3 in Figure 19). For the specimens tested in this study, the distribution of carbon fibers in the grooves were not uniform (Figure 2) [18], with some grooves containing only epoxy while others were filled with both carbon fiber and epoxy. This resulted in the region of the liner affected by the stress concentration to vary between specimens. From the results of grooving simulation 3, it can be deduced that on average, about 50% of the grooves in the GR-C specimens contained carbon fiber. From the experimental and simulation results, it can be seen that having the carbon tows wound into the grooves can improve the liner-composite bonding.

The traction at the onset of damage, τ^o for the liner-composite interface with grooving surface treatment was determined as 6 MPa (Table 8). This value is low compared to the strength of the epoxy resin used, which is 80 MPa. This suggests that the failure at the liner-composite interface is due to slipping at the interface and not due to matrix cracking. The groove depth that was used was too small to prevent this slipping. For liner with a larger thickness, the groove depth can be increased to increase the τ^o for the liner-composite interface. Besides this, the liner-composite bonding can also be further improved by using the grooving surface treatment in conjunction with other surface treatment methods such as etching and anodizing.

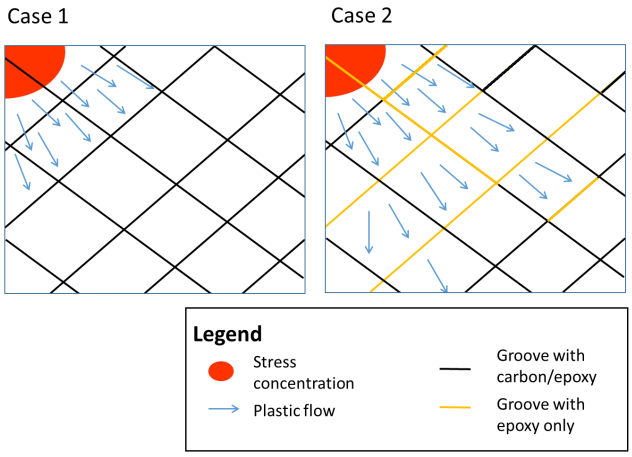

Figure 20: Schematic diagram of plastic deformation in aluminum liner with grooves

5. Conclusions

The effects of two mechanical surface treatment methods for metal liners, grooving and grit blasting, on the metal-composite bonding in composite pipes have been studied. By fitting the FE simulations to experimental data from lateral compression tests, the liner-composite interfacial properties for the grooving and grit blasting treatment methods were determined. The grooving treatment method produced both higher interface stiffness and traction at the onset of failure. This shows that the grooving method is effective in improving the bonding between the aluminum liner and the carbon/epoxy composite.

Using the axial compression experimental results and FE simulations, the effects of the two surface treatment methods on the stress concentration and distribution in the metal liner were also investigated. For the grit blasting treatment, stress concentration in the liner is distributed over the entire length of the specimen. This was successfully simulated using the slanted contact model in FE simulations. On the other hand, the grooving treatment method can help to reinforce the liner by having the fiber tows aligned into the grooves. As a result, yielding of the liner only occurred at the ends of the specimen initially, as compared to the middle region which yielded at a later stage. This effect was successfully captured by introducing the sandwich model concept in FE simulations. The specimens fabricated with the grooving treatment method carried more load before failing compared to the grit blasting method.

In summary, the grooving treatment method was found to improve the metal-composite bonding compared to the grit blasting treatment. For the grooving treatment, it is advisable to have the carbon fiber tows fill in the grooves to provide reinforcement to the metal liner.

Acknowledgements

Y.D. Boon is grateful for the financial support by NTU through the PhD scholarship award.

References

[1] O. O. Ochoa, Composite riser experience and design guidance, Tech. rep., Offshore Technology Research Center, Texas A&M University (2006).

[2] Det Norske Veritas, Recommended practice for composite risers, DNV-RP-F202 (2010).

[3] W. Wu, D. Abliz, B. Jiang, G. Ziegmann, D. Meiners, A novel process for cost effective manufacturing of fiber metal laminate with textile reinforced pCBT composites and aluminum alloy, Composite Structures 108 (2014) 172–180.

[4] Y. B. Hu, H. G. Li, L. Cai, J. P. Zhu, L. Pan, J. Xu, J. Tao, Preparation and properties of fibre-metal laminates based on carbon fibre reinforced pmr polyimide, Composites: Part B 69 (2015) 587–591.

[5] B. Müller, G. Palardy, S. Teixeira de Freitas, J. Sinke, Out-of-autoclave manufacturing of GLARE panels using resistance heating, Journal of Composite Materials (2017). Advance online publication. http://dx.doi.org/10.1177/0021998317727592.

[6] M.-S. Seong, T.-H. Kim, K.-H. Nguyen, J.-H. Kweon, J.-H. Choi, A parametric study on the failure of bonded single-lap joints of carbon composite and aluminum, Composite Structures 86 (2008) 135–145.

[7] B. Blackman, J. P. Dear, A. J. Kinloch, S. Osiyemi, The calculation of adhesive fracture energies from double-cantilever beam test specimens, Journal of Materials Science Letters 10 (1991) 253–256.

[8] G. Lawcock, L. Ye, Y.-W. Mai, C.-T. Sun, The effect of adhesive bonding between aluminum and composite prepreg on the mechanical properties of carbon-fiber-reinforced metal laminates, Composites Science and Technology 57 (1997) 35–45.

[9] G. Reyes V., W. Cantwell, The mechanical properties of fibre-metal laminates based on glass fibre reinforced polypropylene, Composites Science and Technology 60 (2000) 1085–1094.

[10] T. Sinmazçelik, E. Avcu, M. Ö. Bora, O. Çoban, A review: Fibre metal laminates, background, bonding types and applied test methods, Materials and Design 32 (2011) 3671–3685.

[11] S. Teixeira de Freitas, J. Sinke, Adhesion properties of bonded composite-to-aluminum joints using peel tests, The Journal of Adhesion 90 (2014) 511–525.

[12] B. J. Ho, J. K.-H. Tsoi, D. Liu, C. Y.-K. Lung, H.-M. Wong, J. P. Matinlinna, Effects of sandblasting distance and angles on resin cement bonding to zirconia and titanium, International Journal of Adhesion and Adhesives 62 (2015) 25–31.

[13] S. Sharifi Golru, M. M. Attar, B. Ramezanzadeh, Effects of surface treatment of aluminum alloy 1050 on the adhesion and anticorrosion properties of the epoxy coatings, Applied Surface Science 245 (2015) 360–368.

[14] P. He, K. Chen, J. Yang, Surface modifications of Ti alloy with tunable hierarchical structures and chemistry for improved metal-polymer interface used in deepwater composite riser, Applied Surface Science 328 (2013) 614–622.

[15] P. He, K. Chen, B. Yu, C. Y. Yue, J. Yang, Surface microstructures and epoxy bonded shear strength of Ti6Al4V alloy anodized at various temperatures, Composite Science and Technology 82 (2013) 15–22.

[16] Y. Xu, H. Li, Y. Shen, S. Liu, W. Wang, J. Tao, Improvement of adhesion performance between aluminum alloy sheet and epoxy based on anodizing technique, International Journal of Adhesion and Adhesives 70 (2016) 74–80.

[17] P. Molitor, V. Barron, T. Young, Surface treatment of titanium for adhesive bonding of polymer composites: A review, International Journal of Adhesion and Adhesives 21 (2001) 129–136.

[18] Y. D. Boon, S. C. Joshi, L. S. Ong, Effects of mechanical surface treatment on bonding between aluminum and carbon/epoxy composites, in: Procedia Engineering, Vol. 184, 2017, pp. 552–559.

[19] G. Rathnaweera, Y. Durandet, D. Ruan, S. Kinoshita, Characterizing the material properties of a tube from a lateral compression test, International Journal of Protective Structures 2 (2011) 465–476.

[20] ANSYS, Inc., Ansys release 15.0, help system, mechanical APDL theory reference (2013).

[21] Dassault Systemes, Abaqus version 6.14 user's manual (2014).

[22] B. D. Agarwal, L. J. Broutman, K. Chandrashekhara, Analysis and Performance of Fiber Composites, John Wiley & Sons, Inc., New Jersey, United States of America, 2006.

[23] P. P. Camanho, F. L. Matthews, A progressive damage model for mechanically fastened joints in composite laminates, Journal of Composite Materials 33 (1999) 2248–2280.

[24] M. L. Benzeggagh, M. Kenane, Measurement of mixed-mode delamination fracture toughness of unidirectional glass/epoxy composites with mixed-mode bending apparatus, Composites Science and Technology 56 (1996) 439–449.

[25] W. Liu, Y. Huan, J. Dong, Y. Tai, D. Lan, A correction method of elastic modulus in compression tests for linear hardening materials, MRS Communications 5 (2015) 641–645.